Check for updates

Regenerated Graphite Electrodes with Reconstructed Solid Electrolyte Interface and Enclosed Active Lithium Toward >100% Initial Coulombic Efficiency

Yongsheng Ji, Hao Zhang, Dan Yang, Yujun Pan, Zhenglu Zhu, Xiaoqun Qi, Xinpeng Pi, Weichen Du, Zhiheng Cheng, Yonggang Yao, Long Qie,* and Yunhui Huang**

Solid electrolyte interface (SEI) is arguably the most important concern in graphite anodes, which determines their achievable Coulombic efficiency (CE) and cycling stability. In spent graphite anodes, there are already-formed (yet loose and/or broken) SEIs and some residual active lithium, which, if can be inherited in the regenerated electrodes, are highly desired to compensate for the lithium loss due to SEI formation. However, current graphite regenerated approaches easily destroy the thin SEIs and residue active lithium, making their reuse impossible. Herein, this work reports a fast-heating strategy (e.g., 1900 K for ≈150 ms) to upcycle degraded graphite via instantly converting the loose original SEI layer (≈100 nm thick) to a compact and mostly inorganic one (≈10–30 nm thick with a 26X higher Young's Modulus) and still retaining the activity of residual lithium. Thanks to the robust SEI and enclosed active lithium, the regenerated graphite exhibited 104.7% initial CE for half-cell and gifted the full cells with $LiFePO_4$ significantly improved initial CE (98.8% versus 83.2%) and energy density (309.4 versus 281.4 Wh kg^{-1}), as compared with commercial graphite. The as-proposed upcycling strategy turns the "waste" graphite into high-value prelithiated ones, along with significant economic and environmental benefits.

1. Introduction

The success of long-life lithium-ion batteries (LIBs) should give credit to the stable solid electrolyte interface (SEI) formed on the surface of graphite particles, as the SEI suppresses the continuous reduction of the electrolyte and ensures stable cycling in LIBs. However, the formation of the SEI consumes active lithium from the cathodes and thus leads to low initial Coulombic efficiency (CE) and reduced practical energy density for the full cells.[1] Many approaches have been developed in the past years to reduce (e.g., constructing artificial SEI,[2] formulating new electrolytes,[3] etc.) or compensate (e.g., adding prelithiation additives into the cathodes or anodes[4]) the irreversible lithium loss, yet all these approaches rely heavily on external Li sources and inevitably increase the costs and complexity of LIB manufacturing and many are impractical for scalable employment.[5]

Unlike fresh graphite, the cycled graphite in spent batteries has already formed SEIs covering the particle surface and even some residual lithium between the graphite layers. Therefore, it would be highly desired if these SEIs and active lithium could be inherited in the new battery systems, thus to avoid the formation of SEI and compensate lithium loss during cycling. Unfortunately, this is not yet realized in graphite recycling/upcycling. Researchers have developed various methods in spent graphite rejuvenation, such as high-temperature sintering,[6] acid/base immersion,[7] and Joule heat treatment.[8] However, previous methods, either solution or high temperature based, always involve processes such as acid soaking and/or long-time calcination, which almost completely destroy the valuable SEI and residual active lithium, making their reuse impossible. For example, Chen et al. employed ultrahigh temperature (2850 K) to recycle graphite followed by acid leaching, obtaining only carbon-coated graphite yet without surface SEIs (e.g., LiF and Li_2O).[8a]

Meanwhile, although valuable, the SEI from spent electrodes is a mixture of organic–inorganic components (e.g., $ROCO_2Li$, ROLi, and $LiPF_6$)[9] and often evolves into thick and porous layers after repeated charge–discharge cycles, leading to increased impedance/resistance, active lithium consumption, and finally battery failure.[10] Apparently, direct application of spent electrodes with existing SEIs is inappropriate and impractical. Ideally, inorganic SEI could provide higher mechanical durability and ionic conductivity than the randomly distributed organic–inorganic one.[11] In addition, the higher the proportion of inorganic components in SEI, the lower the degree of SEI swelling and the better battery cycling.[12] Therefore, rational and facile construction of robust and inorganic SEI on the graphite surface would be ideal to realize high initial CE, higher energy density,

---

Y. Ji, H. Zhang, D. Yang, Y. Pan, Z. Zhu, X. Qi, X. Pi, W. Du, Z. Cheng, Y. Yao, L. Qie, Y. Huang
State Key Laboratory of Material Processing and Die and Mold Technology
School of Materials Science and Engineering
Huazhong University of Science and Technology
Wuhan, Hubei 430074, China
E-mail: yaoyg@hust.edu.cn; qie@hust.edu.cn; huangyh@hust.edu.cn

The ORCID identification number(s) for the author(s) of this article can be found under https://doi.org/10.1002/adma.202312548

DOI: 10.1002/adma.202312548

© 2024 Wiley-VCH GmbH

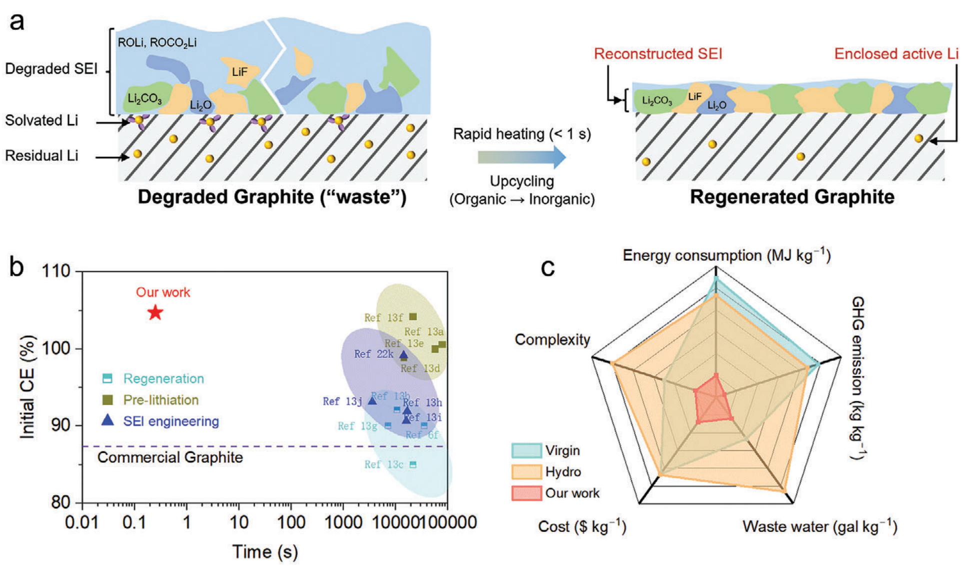

Figure 1. a) Schematic diagram showing the transformation of degraded graphite with loose solid electrolyte interface (SEI) into regenerated graphite with compact one. b) Comparison of manufacturing time and initial Coulombic efficiency (CE) of the graphite regenerated with our rapid direct method with those of C-Gra and other reported recycling and prelithiation or SEI engineering methods. c) Radar map of economic and environmental comparison of manufacturing 1 kg graphite with raw materials (virgin), hydrometallurgical regeneration (hydro), and rapid direct regeneration (our work).

and cycling stability. Currently, none of the reported approaches have attempted to reconstruct the SEI and residual active lithium in degraded graphite electrodes.

Here, we report a direct and fast heating strategy (e.g., 1900 K for ≈150 ms) to upcycle the degraded graphite (D-Gra) electrodes by instantaneously transforming the loose and organic–inorganic SEI to compact and mostly inorganic one (e.g., LiF, Li_2CO_3, Li_2O) covering the graphite surface, along with enclosed active lithium originated from incomplete discharging (e.g., 20% state-of-charge (SOC)), as shown in **Figure** 1a. By taking advantage of the reconstructed SEI and the residual active lithium, the as-proposed regeneration method enables the regenerated graphite (R-Gra) to a high initial CE of 104.7%, much higher than those of the commercial graphite (C-Gra, 87.3%) and other regenerated graphite anodes (Figure 1b), thus eliminating the need of prelithiation. At the same time, the direct regeneration method takes only ≈150 ms to recycle and upgrade spent graphite, much less than those of the reported recycling, prelithiation, or SEI engineering methods (from 2 to 10 h).[6f,13] Compared to the intricate processes required for conventional prelithiation and SEI engineering, our method therefore not only upcycled graphite with artificially engineered and robust SEI toward high-performing anodes, but also enables sustainable recycling of spent anodes, characterized by significantly reduced energy consumption, negligible carbon emissions, and substantial profits (Figure 1c, detailed calculations in Figure 6).

2. Results and Discussion

The D-Gra electrodes were obtained by disassembling the spent mobile phone batteries in a glove box. The as-collected D-Gra electrodes show a yellow–brown color, indicating the lithiated state of the graphite and confirming the presence of the residual active lithium within the graphite owing to incomplete discharge to 20% SOC (Figure S1a, Supporting Information). Due to phase separation in D-Gra and prior lithiation at the surface,[14] D-Gra with a 20% SOC displays a yellow–brown color that typically associated with highly lithiated graphite.[15] The disassembly of the spent LIBs at 20% SOC not only renders more active lithium in the spent graphite for controllable regeneration but also minimizes the generation of Cu impurities compared to fully discharged samples, which has become a new norm in direct recycling industry.[16] Triggered by a voltage-programmable Joule heating setup at a voltage of ≈40 V for ≈150 ms along with natural cooling, a fast-heating treatment was applied to the D-Gra electrode in an argon (Ar) filled glove box. During this process, the active lithium may participate in the SEI reconstruction reactions or evaporate, leading to a reduction of its content, thus the obtained R-Gra electrode is in a black color. It is worth noting that due to the limited size of the homemade device, Figure S1b (Supporting Information) and **Figure** 2a are digital photos of the spent graphite anode after being cutted and subsequently washed with DMC solvent to remove residual lithium salts from the electrolyte.

The morphology of D-Gra and R-Gra was first explored using scanning electron microscopy (SEM). As the SEM images are shown in Figures 2b,c, and Figure S2 (Supporting Information), unlike D-Gra, which presents fragments, R-Gra shows an integrated and dense surface. The composition of D-Gra and R-Gra was studied by X-ray diffraction (XRD). As the results displayed in Figure 2d and Figure S3 (Supporting Information), after the heating process, new peaks belonging to the inorganic components (e.g., LiF, Li_2O, and Li_2CO_3) are detected, indicating the formation of the inorganic SEI in R-Gra. Fourier transform infrared (FTIR) spectroscopy was employed to identify the conversion of the SEI components. As the results shown in Figure 2e, compared with D-Gra, R-Gra only shows two main absorption bands located at 1417 (νC—O) and 864 cm^{-1} (νCO_3^{2-}), corresponding

15214095, 0, Downloaded from https://onlinelibrary.wiley.com/doi/10.1002/adma.202312548 by Shanxi University, Wiley Online Library on [01/04/2024]. See the Terms and Conditions (https://onlinelibrary.wiley.com/terms-and-conditions) on Wiley Online Library for rules of use; OA articles are governed by the applicable Creative Commons License

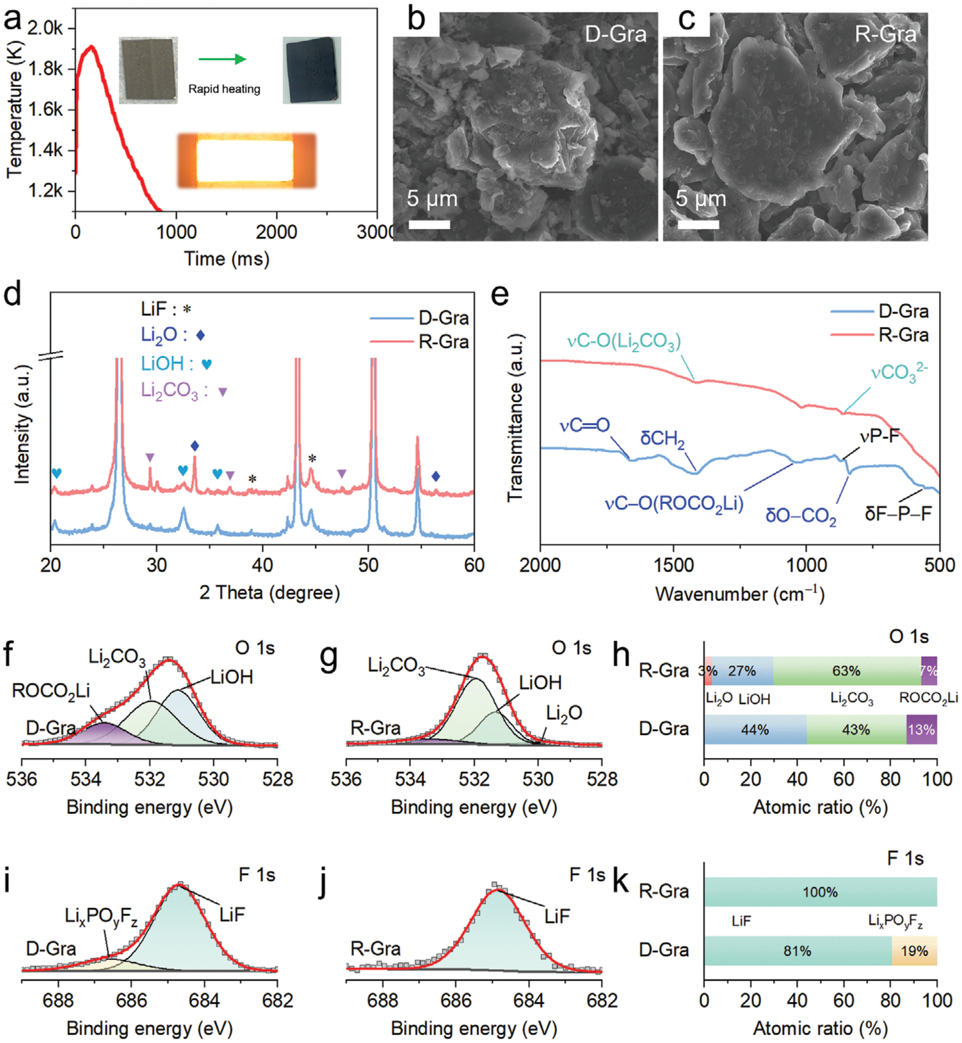

Figure 2. Structural and compositional analysis of the D-Gra and R-Gra electrodes. The temperature–time curve of the rapid heating process (the inset shows the digital photos of D-Gra and R-Gra electrodes and the heating device). Scanning electron microscopy (SEM) images of b) D-Gra and c) R-Gra. d) X-ray diffraction (XRD) patterns and e) Fourier transform infrared (FTIR) spectra of D-Gra and R-Gra. O 1s X-ray photoelectron spectroscopy (XPS) spectra of f) D-Gra and g) R-Gra. The atomic ratio of different h) O chemical states of D-Gra and R-Gra. F 1s XPS spectra of i) D-Gra and j) R-Gra. The atomic ratio of different k) F chemical states of D-Gra and R-Gra.

to the characteristic peaks of Li_2CO_3.[17] While the bands at 1632, 1409, 1300, 1040, and 837 cm^{-1}, which belong to the organic components (e.g., $ROCO_2Li$, and ROLi) disappear,[18] confirming the transformation of the organic SEI components into inorganic ones, which is consistent with the XRD results (Figure 2d).

The conversion of the SEI from organic to inorganic could also be verified by the X-ray photoelectron spectroscopy (XPS, Figures 2f–k and Figure S4, Supporting Information), where the densities of peaks belonging to C—O (287.0 eV) of ROLi, C═O (533.0 eV) of $ROCO_2Li$ decrease, while the one belonging to Li_2CO_3 (531.9 eV) increases. The relevant chemical reaction equation[19] for converting organic components into inorganic components is shown in Note S1 (Supporting Information). The increase of inorganic components in the SEI is beneficial to cycling stability, as shall be discussed later. Thermogravimetry differential scanning calorimetry (TG-DSC) curves of D-Gra and R-Gra in the air atmosphere are shown in Figure S5 (Supporting Information). D-Gra shows a slight mass and heat changes around 554.7 K, which may be ascribed to the conversion of the organic components in the SEI to inorganic ones. Moreover, the rapid heating process also healed the damaged crystal structure of D-Gra, as confirmed by the decreased peak ratio (from 0.18 to 0.14) of the defect band (I_D) to graphite band (I_G) in the Raman spectra (Figure S6, Supporting Information), without damaging the bulk structure of the graphite particles (Figure S7, Supporting Information).

Atomic force microscopy (AFM) was employed to explore the mechanical properties of the SEI of D-Gra and R-Gra (see the measurement details in Figure S8, Supporting Information). The indentation curves record the mechanical response of the SEI layer. As the results shown in **Figures** 3a,b, D-Gra exhibits a distinct double-layer structure with a soft outer layer of >10 nm and a hard inner layer. In contrast, R-Gra displays a single-layer structure, which verifies that the organic layer has been transformed

© 2024 Wiley-VCH GmbH

15214095, 0, Downloaded from https://onlinelibrary.wiley.com/doi/10.1002/adma.202312548 by Shanxi University, Wiley Online Library on [01/04/2024]. See the Terms and Conditions (https://onlinelibrary.wiley.com/terms-and-conditions) on Wiley Online Library for rules of use; OA articles are governed by the applicable Creative Commons License

15214095, 0, Downloaded from https://onlinelibrary.wiley.com/doi/10.1002/adma.202312548 by Shanxi University, Wiley Online Library on [01/04/2024]. See the Terms and Conditions (https://onlinelibrary.wiley.com/terms-and-conditions) on Wiley Online Library for rules of use; OA articles are governed by the applicable Creative Commons License

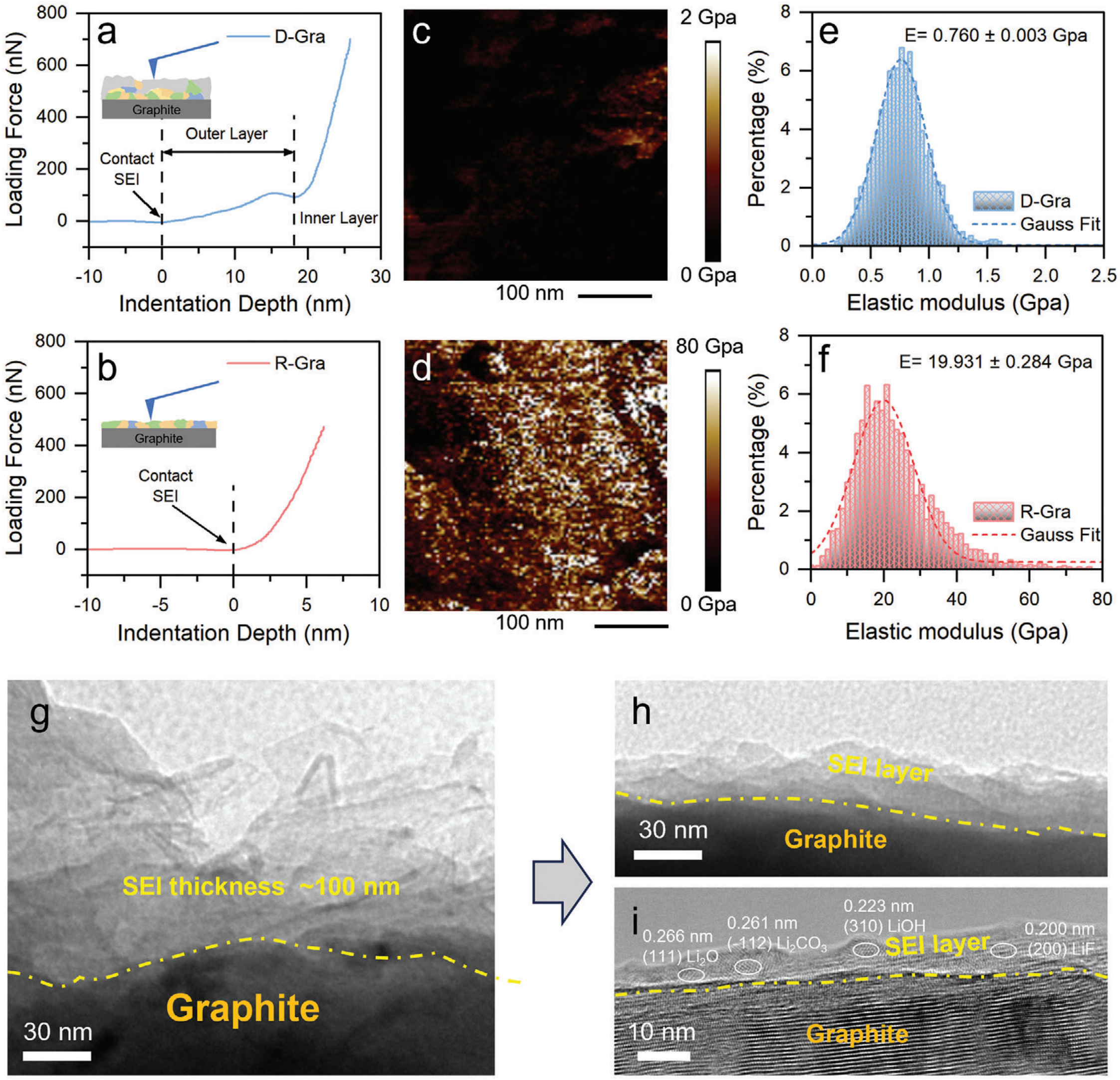

Figure 3. Mechanical properties and morphological evolution of the solid electrolyte interface (SEI) layers of D-Gra and R-Gra. Indentation curves of the SEI of a) D-Gra and b) R-Gra. The two-dimensional Young's modulus maps of c) D-Gra and d) R-Gra. Histograms of the elastic modulus of e) D-Gra and f) R-Gra. Transmission electron microscope (TEM) images of g) D-Gra and h) R-Gra. i) The high-resolution TEM (HRTEM) images of R-Gra.

into a robust and dense inorganic layer.[20] Additionally, the AFM morphology image, as illustrated in Figure S9 (Supporting Information), reveals that compared to D-Gra, the surface of R-Gra is smoother, indicating the reconstruction of SEI on the graphite surface.

Quantitative nanomechanics (QNM) is an extended application mode of AFM that is useful for measuring Young's modulus of SEI. Elastic modulus distribution and Young's modulus mapping diagram are shown in Figures 3c–f. The elastic modulus of R-Gra is 19.931 ± 0.284 Gpa, 26 times that of D-Gra (0.760 ± 0.003 Gpa), such an increase in Young's modulus may be due to the conversion of organic/inorganic to inorganic components after rapid direct regeneration (organic components are softer than inorganic ones).[11a,12] This provides a higher toughness and durability of SEI to tolerate the volume change of graphite during cycling.[21] Moreover, the higher Young's modulus of R-Gra is around 20 GPa, which far exceeds the modulus needed to block the growth of Li dendrite (6 GPa).[22]

We further explored the morphology of D-Gra and R-Gra using the transmission electron microscope (TEM). The TEM images in Figures 3g–i further reveal the conversion of the thick and loose SEI (≈100 nm in thickness) into the thin and dense one (10–30 nm in thickness) after the rapid heating process. Inorganic components (e.g., Li_2O, Li_2CO_3, LiOH, and LiF) are also detected with the high-resolution transmission electron microscope (HRTEM) image (Figure 3i and Figure S10, Supporting Information), which agrees with the results of XRD (Figure 2d). Based on the above results, the SEI constructions of D-Gra and R-Gra are consistent with the structural schematic in Figure 1a, the dense and inorganic SEI of R-Gra may lead to lower swelling and thus provide a prerequisite for stable battery cycling.[12]

The electrochemical behaviors of R-Gra were first investigated and compared with commercial C-Gra and D-Gra in coin cells

15214095, 0, Downloaded from https://onlinelibrary.wiley.com/doi/10.1002/adma.202312548 by Shanxi University, Wiley Online Library on [01/04/2024]. See the Terms and Conditions (https://onlinelibrary.wiley.com/terms-and-conditions) on Wiley Online Library for rules of use; OA articles are governed by the applicable Creative Commons License

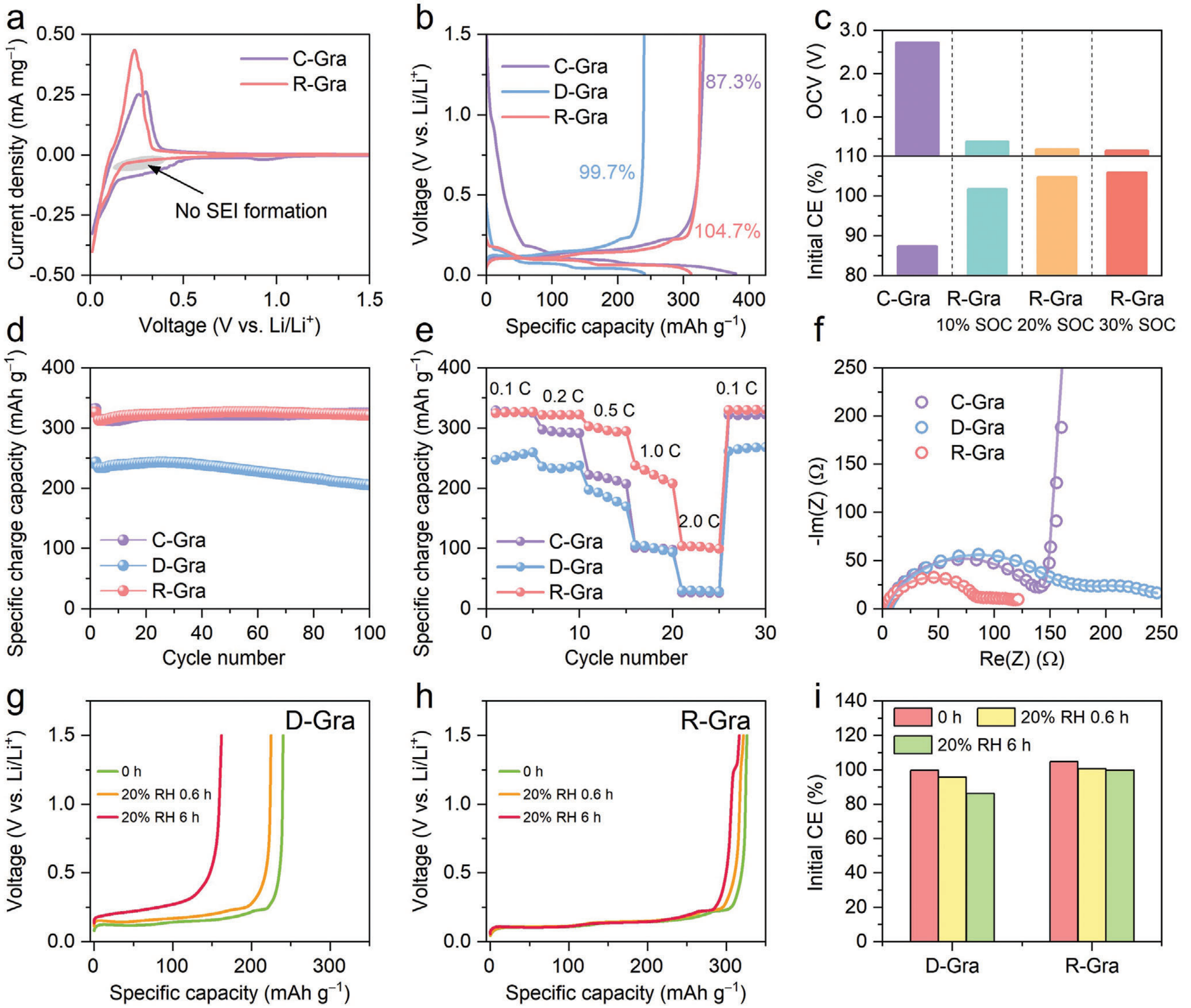

Figure 4. Electrochemical characterizations of Li||C-Gra, Li||D-Gra, and Li||R-Gra cells. a) The initial cyclic voltammetry (CV) curves at a scan rate of 0.1 mV s^{-1}. b) The initial charge–discharge profiles at 0.1 C. c) The open-circuit voltage (OCV) and initial Coulombic efficiencies (CEs) of C-Gra and R-Gra with different state-of-charge (SOC). d) Cycling performance at 0.2 C (0.1 C for the initial two cycles). e) Rate performance at 0.1 to 2 C. f) Nyquist plots of the fresh cells. g,h) The initial charge curve of Li||D-Gra and Li||R-Gra cell with the electrode being exposed to air for 0, 0.6, and 6 h. i) The initial CEs of D-Gra and R-Gra after different exposure times.

using Li-metal as the counter electrodes. As the cyclic voltammetry (CV) curves displayed in **Figure 4**a, the Li||C-Gra cell shows a typical reduction peak at <0.5 V, which could be assigned to the formation of SEI on the surface of graphite particles in the initial cycle. Additionally, the CV curve of HR-Gra also exhibits a noticeable reduction peak (Figure S11, Supporting Information), indicating that prolonged exposure to high temperatures can compromise the integrity of the SEI structure.[23] In contrast, with R-Gra electrodes, no obvious SEI formation peak (marked position in Figure 4a) is observed, indicating the as-inherited SEI from D-Gra functions well in preventing electrolyte reduction.

The initial charge–discharge curves of C-Gra, D-Gra, and R-Gra half cells at 0.1 C (1 C = 372 mA g^{-1}) are shown in Figure 4b. Compared with the C-Gra cell, there is negligible capacity contribution belonging to the SEI formation during discharging (in the voltage range from 1.0 to 0.2 V) for both the cells with D-Gra and R-Gra electrodes (Figure 4b), which is consistent with the CV curves (Figure 4a). Figure 4c provides a summary of the initial potential profiles of C-Gra and R-Gra under different SOC conditions, encompassing the initial open-circuit voltages (OCVs) and initial Coulombic efficiencies (CEs). In the case of Li||R-Gra cell, the CEs tend to increase while the OCVs tend to decrease with improved SOC.[4c] Furthermore, the discharge process free of SEI formation enables remarkably high CEs for D-Gra (99.7%) and R-Gra (101.6% for 10% SOC, 104.7% for 20% SOC, and 105.8% for 30% SOC), which are substantially higher than that of C-Gra (87.3%). Among the R-Gra samples, the highest specific charge capacity is observed for R-Gra with 20% SOC (326.3 mAh g^{-1}),

© 2024 Wiley-VCH GmbH

15214095, 0, Downloaded from https://onlinelibrary.wiley.com/doi/10.1002/adma.202312548 by Shanxi University, Wiley Online Library on [01/04/2024]. See the Terms and Conditions (https://onlinelibrary.wiley.com/terms-and-conditions) on Wiley Online Library for rules of use; OA articles are governed by the applicable Creative Commons License

surpassing R-Gra with 10% SOC (318.9 mAh g^{-1}) and 30% SOC (307.5 mAh g^{-1}). The CE of R-Gra exceeding 100% can be attributed to two factors: i) the SEI inherited from D-Gra hinders electrolyte decomposition; ii) residual active lithium in D-Gra partially survives during the rapid heating treatment and contributes to the charge capacity.

To further ascertain the optimal heat treatment conditions, we investigated the electrochemical performance of directly regenerated graphite anodes under various conditions. As shown in Figure S12 (Supporting Information), the initial CE rises from 1300 to 1500 K and then declines from 1500 to 1900 K. On the other hand, the specific capacity of the regenerated graphite increases with the increase of the treatment temperature. However, even higher heating (e.g., >2000 K) or much longer operation (e.g., 1000 K for 3 min) may lead to severe side reactions, such as degradation of Cu current collector at higher temperature (Figures S13 and S14, Supporting Information) or significant loss of active lithium during prolonged reaction time. This result not only highlights the importance of transient heating to avoid severe side reactions and active lithium loss but also opens up possibilities for further optimization in the direct regeneration of spent graphite with unique combination of initial CE and capacities.

The active lithium content was calculated through the assembly of Li||R-Gra cells, recording the initial delithiation (charge) curve (Figure S15, Supporting Information). Li||D-Gra and Li||R-Gra cells exhibit capacities of 54.9 and 24.5 mAh g^{-1}, respectively, indicating an approximate 55% of active lithium is converted during the heat treatment at 1900 K for 150 ms (Figure S16, Supporting Information). This conversion can be attributed to a combination of thermal evaporation of a portion of active lithium and its participation in reactions forming a new SEI (Note S1, Supporting Information and Equations S2 and S3). The high CE of R-Gra reduces the consumption of active lithium in the full cells, thereby increasing the actual energy density of the practical cells, which will be discussed later. On the other hand, the specific charge capacity of R-Gra (326.3 mAh g^{-1}) is much higher than that of D-Gra (241.5 mAh g^{-1}), indicating that the rapid heating treatment repairs the damaged structure and dredges the blocked lithium-ion transport channel of the D-Gra particles. The cycling stability of C-Gra, D-Gra, and R-Gra at 0.2 C is compared in Figure 4d (0.1 C for the initial two cycles as the formation process). R-Gra delivers the desired cycling stability (Table S1, Supporting Information) with a capacity retention rate of ≈100% and a specific charge capacity of 321.5 mAh g^{-1} at the 100th cycle, which is comparable with C-Gra (318.1 mAh g^{-1} and ≈100%) but much better than D-Gra (205.5 mAh g^{-1} and ≈87.8%), These results further demonstrate the superb durability of the reconstructed SEI of R-Gra. In addition, R-Gra shows the best rate capability among the three samples. As the rate performance from 0.1 to 2 C shown in Figure 4e, R-Gra delivers specific charge capacities of 324.6, 302.7, 237.9, and 104.4 mAh g^{-1} at 0.1, 0.5, 1.0, and 2.0 C (Figure 4d), much higher than those of C-Gra and D-Gra. The superb rate performance of Li||R-Gra cell could be ascribed to reconstructed SEI, predominantly composed of inorganic components with low desolvation energy barriers,[24] which facilitate enhanced lithium-ion diffusion kinetics. This is consistent with the results of GITT (Figure S17, Note S2, and Table S2, Supporting Information) and electrochemical impedance spectroscopy (EIS) (Figure 4f and Figure S18, Supporting Information).

Concerning the practical applications of R-Gra, one of the key considerations is its air stability due to the presence of electrochemically active lithium. To address this concern, we conducted experiments involving the exposure of D-Gra and R-Gra electrodes to air with a relative humidity of 20% for different durations (0, 0.6, and 6 h). The electrochemical behaviors of Li||D-Gra and Li||R-Gra cells were investigated. Figure 4g depicts the initial charge curve of D-Gra. As the exposure time to air increases from 0 to 6 h, air-exposed D-Gra experiences a significant decrease in charge capacity and initial CE. Specifically, the charge capacity drops from 240.1 to 161.9 mAh g^{-1}, while the initial CE decreases from 99.7% to 86.3%. In contrast, after being exposed to air for 6 h, R-Gra exhibits an initial capacity of 316.5 mAh g^{-1} and an initial CE of 99.6%, slightly lower than the values for fresh R-Gra (326.3 mAh g^{-1} and 104.7%). This slight decrease can be ascribed to the reaction between a fraction of the active lithium and ambient moisture. However, the majority of the active lithium is encapsulated by an organic SEI, effectively isolating it from external moisture and ensuring its preservation. The superior air stability of R-Gra can be attributed to the presence of a dense SEI layer on the surface of R-Gra particles.[25] This stability surpasses that of prelithiated graphite prepared using traditional prelithiation methods.[13j,26] The robust air stability of R-Gra ensures its practical applicability as an electrode material with prelithiation capability.

To further verify the advantages of R-Gra for practical applications, we assembled full cells with industry-level $LiFePO_4$ cathodes (LFP, areal mass loading: 13.2 mg cm^{-2}) cathodes. The schematic diagram of the R-Gra||LFP cell is shown in **Figure 5**a, and the blue spheres between graphite layers represent the residual active lithium in R-Gra, which could compensate for the lithium loss of the full cells during the electrochemical cycles. For R-Gra electrodes, there is no SEI formation peak of the R-Gra full cell in the CV curve (Figure S19, Supporting Information), which is consistent with the CV results in Figure 4a. Moreover, the normalized initial charge–discharge curves of the Li||LFP, Li||C-Gra, and Li||R-Gra cells were used to demonstrate the benefits of upgraded SEI and the reuse of the residual active lithium in R-Gra electrodes (Figure 5b). In C-Gra electrodes, there is always irreversible lithium loss due to the formation of SEI in the initial cycle.[27] In contrast, R-Gra electrodes could even provide additional active lithium due to the SEI-formation-free process and the residual active lithium between the graphite layers. On the other hand, the LFP electrode also shows an irreversible lithium loss, which may be attributed to the formation of cathode–electrolyte interphase (CEI). Thanks to the high CE of R-Gra, the R-Gra||LFP cell delivers a high initial specific discharge capacity of 143.9 mAh g^{-1} with a high initial CE of 98.8%, significantly higher than those of the cells using C-Gra and D-Gra electrodes (Figure 5c). Remarkably, the R-Gra||LFP cell demonstrates an initial energy density of 309.4 Wh kg^{-1} (Figure 5d), which is higher than C-Gra (281.4 Wh kg^{-1}), and D-Gra (232.3 Wh kg^{-1}), confirming the effectiveness of R-Gra in reducing the SEI formation and compensating the lithium loss of the full cells.

As shown in Figure 5e, the R-Gra||LFP cell shows an excellent rate capability and delivers high discharge capacities of 143.5, 140.1, 135.2, 128.1, and 115.8 mAh g^{-1}, respectively, at 0.1, 0.2,

© 2024 Wiley-VCH GmbH

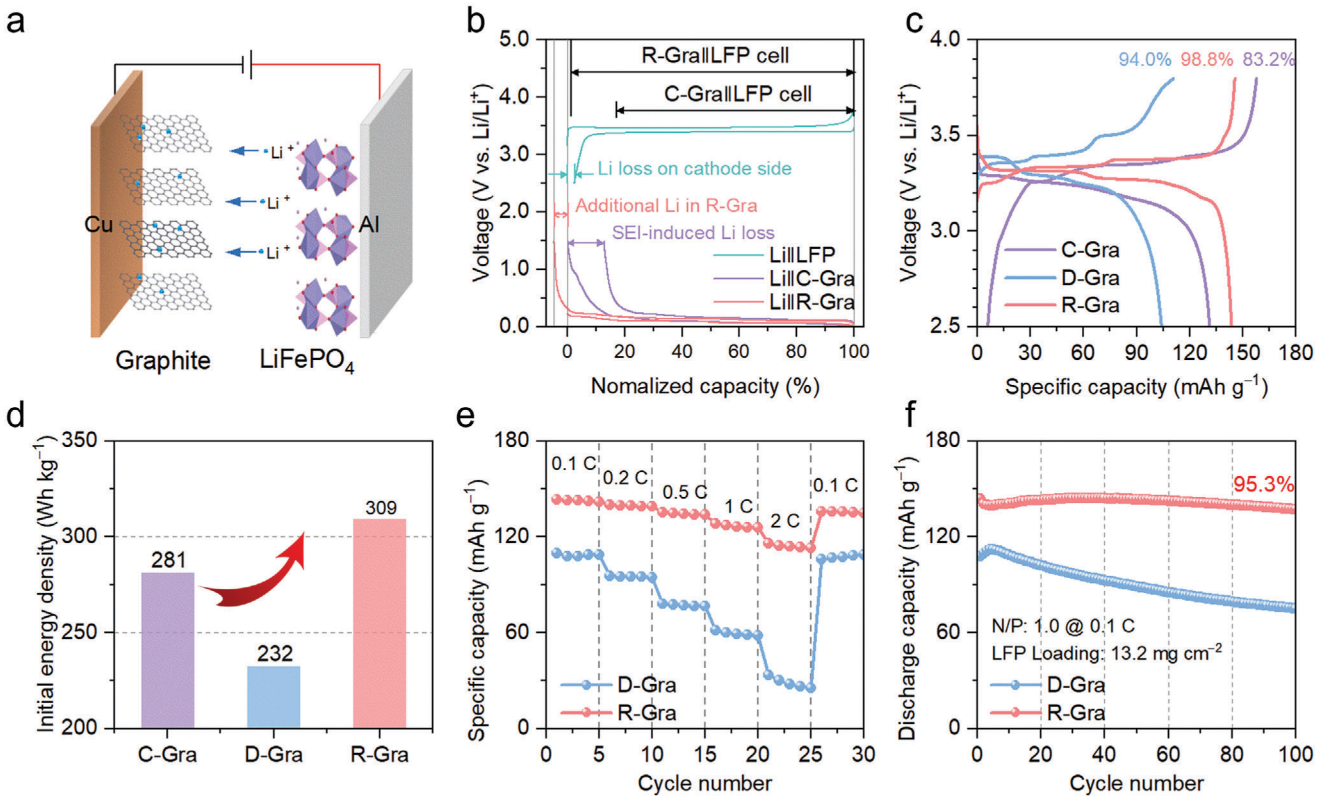

Figure 5. Electrochemical performance of C-Gra||LFP, D-Gra||LFP, and R-Gra||LFP cells. a) Schematic diagram of R-Gra||LFP cell composition (with preintercalated active lithium). b) The normalized charging–discharging curves of C-Gra, R-Gra, and LFP half cells. c) The initial charge–discharge curves at 0.1 C. d) The comparison of the energy density at the initial cycle (calculated based on the mass of the cathode and anode only). e) Rate performance from 0.1 to 2 C. f) Cycle performance at 0.1 C.

0.5, 1, and 2 C. The superb rate performance of R-Gra||LFP cell could be ascribed to the lowest surface film resistance R_{sf} and charge transfer resistance R_{ct} (Figure S20, Supporting Information). Additional, Figure 5f compares the cycling stability of the full cells with D-Gra, and R-Gra electrodes at 0.1 C (1 C = 170 mA g^{-1}). The R-Gra||LFP cell shows an initial specific discharge capacity of 145.0 mAh g^{-1} with a capacity retention of 95.3% after 100 cycles. In sharp contrast, the capacity retention of the D-Gra||LFP cells is 69.5%. Overall, the compact and robust inorganic SEI possesses excellent mechanical properties and plays a decisive role in maintaining the cycling stability of graphite anode. Compared with D-Gra||LFP cell, the improved Coulombic efficiencies of R-Gra||LFP cell (Figure S21, Supporting Information) during the cycling should be attributed to the exceptional stability of the reconstructed SEI. In addition, in order to further prove the improved cycle stability, we conducted a longer cycle performance of R-Gra||LFP cell at 0.2 C (Figure S22, Supporting Information). After 300 cycles, the R-Gra||LFP cell still shows a capacity retention of 92.2%, which is comparable or better than other cells composed of recycled materials (Table S1, Supporting Information).[13b,28] For practical application, despite the achievement of a high initial CE and improved rate performance and energy density, we acknowledge concurrently that there remains a discernible gap in the cycling performance between the regenerated graphite anodes and commercial counterparts in industry, which may be caused by factors such as the degraded structure and impurities. To also achieve outstanding and extended cycling for these directly recycled materials, further significant efforts are required in future studies.

The economic and environmental benefits of the as-proposed direct recycling method were further analyzed with Everbatt 2020 model.[29] As the schematic shown in **Figure 6**a, traditional hydrometallurgy and pyrometallurgy methods always include high-temperature smelting and acid/alkali leaching processes, which are energy-consuming and environmentally unfriendly. In contrast, after proper pretreatment (i.e., battery disassembly along with electrolyte cleaning), our method can effectively regenerate and upcycle the spent graphite without using any solvents. At present, equipment companies are actively developing automatic disassembly devices for pouch cells in an inert environment to minimize harmful effects and potential hazards to the personnel and environment during battery disassembly (Figure S23, Supporting Information). By further companying our Joule heat treatment device, the continuous and direct regeneration of spent graphite anodes can be achieved (Figure S24, Supporting Information). The cost and revenue, profit, energy consumption, greenhouse gas (GHG) emission, and water consumption of manufacturing 1 kg graphite from virgin, hydrometallurgical, and rapid direct regeneration methods are summarized in Figures 6b–f. Obtaining higher environmental and economic benefits in the battery recycling process are indispensable to ensure the sustainability of the recycling industry. For our rapid

© 2024 Wiley-VCH GmbH

15214095, 0, Downloaded from https://onlinelibrary.wiley.com/doi/10.1002/adma.202312548 by Shanxi University, Wiley Online Library on [01/04/2024]. See the Terms and Conditions (https://onlinelibrary.wiley.com/terms-and-conditions) on Wiley Online Library for rules of use; OA articles are governed by the applicable Creative Commons License

15214095, 0, Downloaded from https://onlinelibrary.wiley.com/doi/10.1002/adma.202312548 by Shanxi University, Wiley Online Library on [01/04/2024]. See the Terms and Conditions (https://onlinelibrary.wiley.com/terms-and-conditions) on Wiley Online Library for rules of use; OA articles are governed by the applicable Creative Commons License

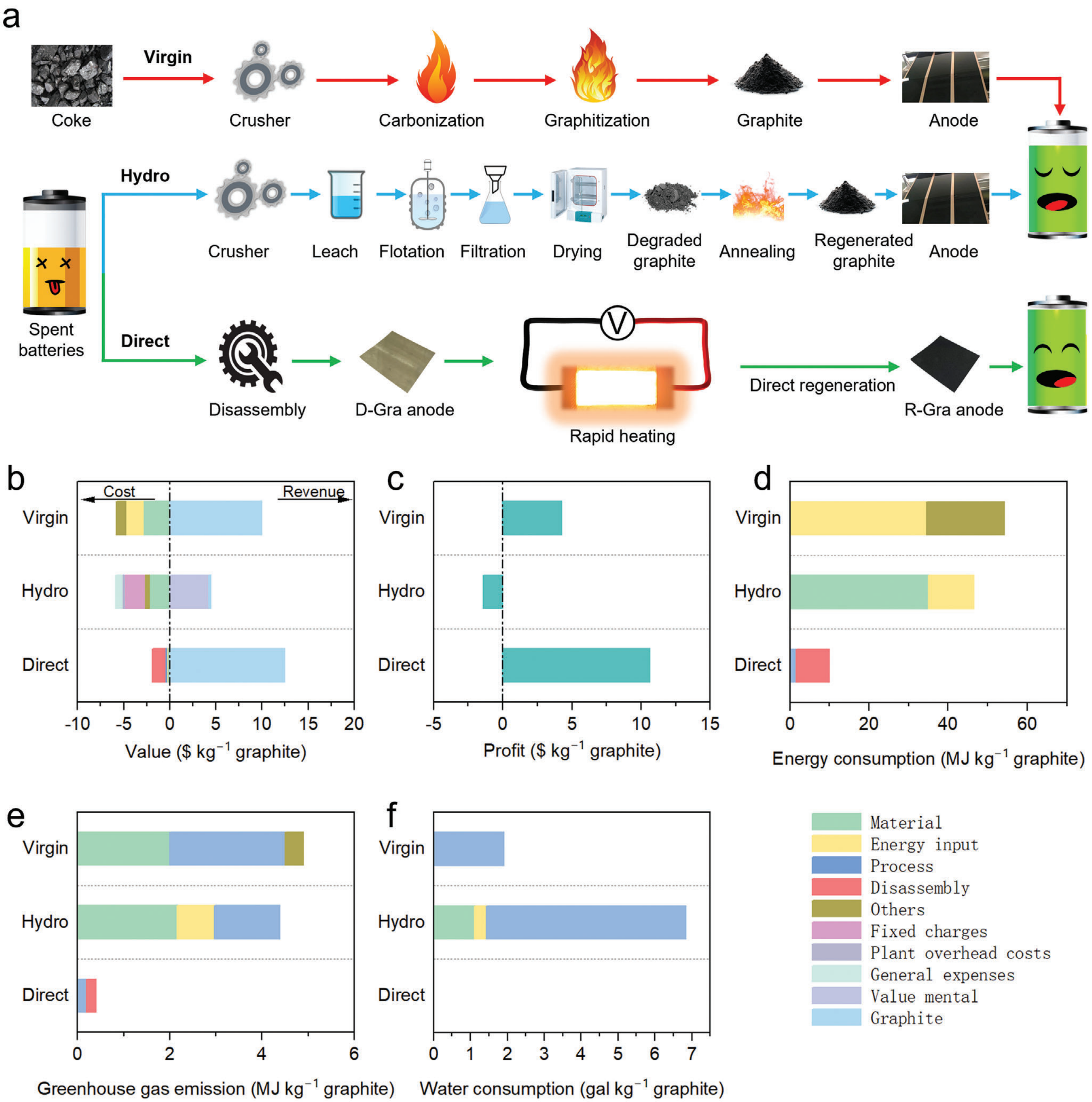

Figure 6. Economic and environmental analysis. a) Schematic diagram showing the manufacturing of lithium-ion batteries (LIBs) with graphite anodes produced from virgin materials (Virgin) and hydrometallurgical (Hydro) and our rapid direct regeneration (Direct) methods. b) Cost and revenue, c) profit, d) total energy consumption, e) greenhouse gas (GHG) emissions, and f) water consumption of manufacturing 1 kg graphite via virgin, hydro, and direct methods.

direct regeneration methods, the expenses associated with battery disassembly primarily encompass the costs of automated disassembly equipment, labor, and consumables. The disassembly cost amounts to \$1.39 Kg^{-1} of graphite, comprising labor costs of \$0.80 kg^{-1}, equipment depreciation of \$0.53 kg^{-1}, and operational electricity expenses of \$0.06 kg^{-1}. Compared with the manufacturing graphite from the hydrometallurgical method, our rapid direct regeneration method reduces recycling cost by ≈68% (Figure 6b), energy consumption by ≈79% (Figure 6d), GHG emission by ≈91% (Figure 6e), and water consumption by 100% (Figure 6f).

Such reductions could be attributed to the shorter recycling process and lower electricity consumption. Additionally, unlike those reported methods for degraded graphite,[8a] our rapid direct regeneration method obtains upcycled graphite anodes, eliminating the need for complex coating processes and offering additional reductions in energy consumption and environmental pollution. Furthermore, compared with the manufacturing of graphite from virgin materials, our rapid direct regeneration method reduces the cost by ≈67%, energy consumption by ≈82%, GHG emission by ≈92%, and water consumption by 100%. Notably, the profit of graphite recycling by hydrometallurgy is negative, which is why few researchers are interested in recycling spent graphite. In sharp contrast, our rapid direct regeneration method can achieve a profit of \$10.6 kg^{-1} (Figure 6c), which is significantly higher than the method of producing graphite from raw materials (\$3.3 kg^{-1}). On the other hand, our regenerated graphite electrode shows a higher energy density than the pristine commercial graphite electrode (309.4 versus 281.4 Wh kg^{-1}), as verified by the comparison of the energy density in Figure 5d. Therefore, our rapid direct regeneration method can not only improve the environmental and economic benefits but also significantly enhance the energy density of regenerated graphite full cells.

3. Conclusion

In this study, we present a simple and efficient rapid heating treatment designed to upcycle degraded graphite electrodes within an impressive timeframe of ≈150 ms. Through rapid heating, the loose organic–inorganic SEI in D-Gra transforms into a compact and robust inorganic SEI. The reconstructed SEI also protects the activity of enclosed lithium with largely improved air stability. As a consequence, our approach leads to a high Coulombic efficiency, stable cycling performance, and increased energy density in full cells. Importantly, compared with manufacturing graphite from the hydrometallurgical method, our proposed direct regeneration method yields a substantial reduction in total energy consumption and in GHG emissions. Therefore, our regeneration strategy not only offer an innovative solution for the upcycling of degraded graphite into valuable prelithiated anodes but also holds significant potential to drive the closed-loop sustainability of batteries and particularly the graphite anodes.

4. Experimental Section

Preparation of D-Gra and R-Gra Anodes: The degraded graphite (D-Gra) anodes were obtained by disassembling the spent $LiCoO_2$ cells (5 Ah pouch cell, received from Wuhan Sunmoon Battery Co., Ltd.) at a SOC of 20% with ≈60% of their designed capacity remained in a glove box filled with Ar (Unless specified otherwise, D-Gra is acquired through the disassembly of pouch batteries with a SOC of 20%). The D-Gra electrodes were washed with dimethyl carbonate (DMC) to remove residual electrolytes and dried naturally in a glove box. Next, the D-Gra electrodes were placed on a homemade Joule heating device, heated under a ≈40 V DC power supply for ≈150 ms in a glove box filled with Ar, and finally cooled naturally to room temperature to obtain regenerated graphite (R-Gra) electrodes. The graphite obtained from spent anode material, undergoing a 2-h heat treatment at 773.2 K under an Ar atmosphere, is denoted as high-temperature recycled graphite (HR-Gra). For comparison, commercial graphite electrodes (C-Gra) were fabricated using a mass ratio of graphite:SP:SBR:CMC = 96:2:1:1, and an area loading of approximately ≈6.5 mg cm^{-2}. The air stability test was conducted in an air environment with a relative humidity of 20%.

Characterizations: XRD patterns were collected on a Bruker D8 ADVANCE diffractometer with Cu Kα radiation (λ = 1.5405 Å) with a diffraction angle range of 10° to 80°. The morphologies of D-Gra and R-Gra were characterized using a field emission SEM (JEOL, JSM-7610F Plus). A HRTEM was used to investigate the morphology and crystal structure information of D-Gra and R-Gra. X-ray photoelectron spectra (XPS) were collected on ESCALAB 250Xi with Al Kα (1486.7 eV) irradiation. Raman spectra were collected on LabRAM HR Evolution. FTIR spectra were collected on Nicolet iS50R. The surface morphology and mechanical elasticity of SEI were investigated with an AFM (Nanoscope V Multimode 8 scanning probe microscope, Brucker Dimension Icon) in tapping mode over an area of 1 × 1 µm. The elastic moduli of the SEI of D-Gra and R-Gra were determined by fitting the force-depth curves with the Derjaguin–Müller–Toporov (DMT) model. Young's modulus data were obtained using NanoScope Analysis software. Thermogravimetric analysis was carried out by a TG-DSC (STA 8000, PerkinElmer) in the air with a heating rate of 10 °C min^{-1}. The surface area and pore size were calculated by the Brunauer–Emmett–Teller (BET) method and the Barrett–Joyner–Halenda (BJH) method using the specific surface area and porosity analyzer (Quantachrome, Autosorb iq2-MP).

Electrochemical Measurements: The anodes were fabricated by cutting the waste graphite anode into a circle with a diameter of 12 mm. The areal graphite mass loading of as-prepared anodes was ≈13 mg cm^{-2}. The electrochemical performance was obtained with 2025-type coin cells assembled with lithium chips (Φ15.6 × 0.45 mm, China Energy Lithium Co., Ltd) as an anode, polypropylene membrane (PP, Celgard 2500) as a separator, 1.0 M $LiPF_6$ in ethyl carbonate/diethylene carbonate (EC:DEC = 1:1 by volume) with 5.0% fluoroethylene carbonate additive (DodoChem) as the electrolyte in an Ar-filled glovebox. The galvanostatic charge–discharge measurements were carried out on a NEWARE (CT4008) tester within the voltage range of 0.01 to 1.5 V at different rates. CV curves were collected on an electrochemical workstation (Biological VMP-3) at a scanning rate of 0.1 mV s^{-1}. EIS was collected on an electrochemical workstation (Biological VMP-3) within a range of 0.1 Hz to 100 KHz.

Supporting Information

Supporting Information is available from the Wiley Online Library or from the author.

Acknowledgements

This work was supported by the National Key R&D Program of China (2021YFA1202300), Natural Science Foundation of Hubei Province, China (2022CFA031), the Interdisciplinary Research Program of Huazhong University of Science and Technology (2023JCYJ004), and the Fundamental Research Funds for the Central Universities (2021GCRC001 and 2021GCRC046). The authors thank the test support from the Analytical and Testing Center of Huazhong University of Science and Technology and the State Key Laboratory of Materials Processing and Die and Mould Technology.

Conflict of Interest

The authors declare no conflict of interest.

Author Contributions

Y.J. and H.Z. contributed equally to this work. Y.J., H.Z., L.Q., Y.Y., and Y.H. performed conceptualization. Y.J. and H.Z. performed methodology. Y.J. and H.Z. performed investigation. Y.J., H.Z., Y.D., Y.P., Y.J., Z.Z., and X.Q. conducted formal analysis. X.P., W.D., and Z.C. performed data curation. Y.J. wrote the original draft. . Y.J., H.Z., L.Q., Y.Y., and Y.H. reviewed and edited the writing. L.Q. and Y.Y. performed funding acquisition. Y.J., H.Z., L.Q., Y.Y., and Y.H. provided resources. L.Q., Y.Y., and Y.H. supervised the work.

© 2024 Wiley-VCH GmbH

15214095, 0, Downloaded from https://onlinelibrary.wiley.com/doi/10.1002/adma.202312548 by Shanxi University, Wiley Online Library on [01/04/2024]. See the Terms and Conditions (https://onlinelibrary.wiley.com/terms-and-conditions) on Wiley Online Library for rules of use; OA articles are governed by the applicable Creative Commons License

15214095, 0, Downloaded from https://onlinelibrary.wiley.com/doi/10.1002/adma.202312548 by Shanxi University, Wiley Online Library on [01/04/2024]. See the Terms and Conditions (https://onlinelibrary.wiley.com/terms-and-conditions) on Wiley Online Library for rules of use; OA articles are governed by the applicable Creative Commons License

Data Availability Statement

The data that support the findings of this study are available from the corresponding author upon reasonable request.

Keywords

battery recycling, Coulombic efficiency, graphite upcycling, SEI reconstruction, transient heating

Received: November 22, 2023
Revised: February 1, 2024
Published online:

---

[1] a) H. Adenusi, G. A. Chass, S. Passerini, K. V. Tian, G. Chen, *Adv. Energy Mater.* **2023**, *13*, 2203307; b) D. Y. Wang, N. N. Sinha, R. Petibon, J. C. Burns, J. R. Dahn, *J. Power Sources* **2014**, *251*, 311.

[2] a) Y. Gao, Z. Yan, J. L. Gray, X. He, D. Wang, T. Chen, Q. Huang, Y. C. Li, H. Wang, S. H. Kim, T. E. Mallouk, D. Wang, *Nat. Mater.* **2019**, *18*, 384; b) J. Sun, S. Zhang, J. Li, B. Xie, J. Ma, S. Dong, G. Cui, *Adv. Mater.* **2023**, *35*, 2209404; c) P. Zhai, L. Liu, X. Gu, T. Wang, Y. Gong, *Adv. Energy Mater.* **2020**, *10*, 2001257; d) Y. Sun, K. Zhang, R. Chai, Y. Wang, X. Rui, K. Wang, H. Deng, H. Xiang, *Adv. Funct. Mater.* **2023**, *33*, 2303020; e) J. Seo, S. Hyun, J. Moon, J. Y. Lee, C. Kim, *ACS Appl. Energy Mater.* **2022**, *5*, 5610; f) F. Zou, H. C. Nallan, A. Dolocan, Q. Xie, J. Li, B. M. Coffey, J. G. Ekerdt, A. Manthiram, *Energy Storage Mater.* **2021**, *43*, 499.

[3] X. Fan, L. Chen, O. Borodin, X. Ji, J. Chen, S. Hou, T. Deng, J. Zheng, C. Yang, S.-C. Liou, *Nat. Nanotechnol.* **2018**, *13*, 715.

[4] a) L. Jin, C. Shen, Q. Wu, A. Shellikeri, J. Zheng, C. Zhang, J. P. Zheng, *Adv. Sci.* **2021**, *8*, 2005031; b) Y. Sun, H.-W. Lee, Z. W. Seh, N. Liu, J. Sun, Y. Li, Y. Cui, *Nat. Energy* **2016**, *1*, 15008; c) J. Lee, D. Jin, J. Y. Kim, Y. Roh, H. Lee, S. H. Kang, J. Choi, T. Jo, Y. G. Lee, Y. M. Lee, *Adv. Energy Mater.* **2023**, *13*, 2300172; d) C. Yang, H. Ma, R. Yuan, K. Wang, K. Liu, Y. Long, F. Xu, L. Li, H. Zhang, Y. Zhang, X. Li, H. Wu, *Nat. Energy* **2023**, *8*, 703.

[5] X. B. Cheng, R. Zhang, C. Z. Zhao, F. Wei, J. G. Zhang, Q. Zhang, *Adv. Sci.* **2016**, *3*, 1500213.

[6] a) Y. Chen, X. Wen, X. Zhang, C. Yang, L. Wang, L. Zhou, Z. Li, H. Deng, J. Li, *J. Mater. Sci.: Mater. Electron.* **2023**, *34*, 1518; b) D. Yang, Y. Yang, H. Du, Y. Ji, M. Ma, Y. Pan, X. Qi, Q. Sun, K. Shi, L. Qie, *Green Energy Environ.* **2022**; c) H. Da, J. Li, J. Shi, H. Zhang, *Carbon* **2022**, *193*, 157; d) S. Natarajan, K. Krishnamoorthy, A. Sathyaseelan, V. K. Mariappan, P. Pazhamalai, S. Manoharan, S.-J. Kim, *Nano Energy* **2022**, *101*, 107595; e) Y. Gao, J. Zhang, H. Jin, G. Liang, L. Ma, Y. Chen, C. Wang, *Carbon* **2022**, *189*, 493; f) Y. Li, W. Lv, H. Zhao, Y. Xie, D. Ruan, Z. Sun, *Green Chem.* **2022**, *24*, 9315; g) N. Yao, F. Liu, Y. Zou, H. Wang, M. Zhang, X. Tang, Z. Wang, M. Bai, T. Liu, W. Zhao, R. Xue, Y. Liu, Y. Ma, *Energy Storage Mater.* **2023**, *55*, 417.

[7] H. Da, W. Fang, J. Zhu, J. Li, S. Pan, J. Li, J. Huang, H. Zhang, S. Zhang, *Small* **2023**, *19*, 2304060.

[8] a) W. Chen, R. V. Salvatierra, J. T. Li, C. Kittrell, J. L. Beckham, K. M. Wyss, N. La, P. E. Savas, C. Ge, P. A. Advincula, *Adv. Mater.* **2023**, *35*, 2207303; b) J. Luo, J. Zhang, Z. Guo, Z. Liu, S. Dou, W.-D. Liu, Y. Chen, W. Hu, *Nano Res.* **2023**, *16*, 4240; c) H. Zhang, Y. S. Ji, Y. G. Yao, L. Qie, Z. H. Cheng, Z. H. Ma, X. Qian, R. G. Yang, C. H. Li, Y. Q. Guo, Y. F. Yuan, H. Y. Xiao, H. P. Yang, J. Ma, J. Lu, Y. H. Huang, *Energy Environ. Sci.* **2023**, *16*, 2561; d) Z. Cheng, Z. Luo, H. Zhang, W. Zhang, W. Gao, Y. Zhang, L. Qie, Y. Yao, Y. Huang, K. K. Fu, *Carbon Energy* **2023**, e395; e) S. Dong, Y. Song, K. Ye, J. Yan, G. Wang, K. Zhu, D. Cao, *EcoMat* **2022**, *4*, e12212.

[9] N. Takenaka, A. Bouibes, Y. Yamada, M. Nagaoka, A. Yamada, *Adv. Mater.* **2021**, *33*, 2100574.

[10] a) J. Vetter, P. Novák, M. R. Wagner, C. Veit, K.-C. Möller, J. Besenhard, M. Winter, M. Wohlfahrt-Mehrens, C. Vogler, A. Hammouche, *J. Power Sources* **2005**, *147*, 269; b) B. Han, Y. Zou, G. Xu, S. Hu, Y. Kang, Y. Qian, J. Wu, X. Ma, J. Yao, T. Li, *Energy Environ. Sci.* **2021**, *14*, 4882.

[11] a) Y. Li, Y. Li, A. Pei, K. Yan, Y. Sun, C. L. Wu, L. M. Joubert, R. Chin, A. L. Koh, Y. Yu, J. Perrino, B. Butz, S. Chu, Y. Cui, *Science* **2017**, *358*, 506; b) H.-H. Sun, A. Dolocan, J. A. Weeks, R. Rodriguez, A. Heller, C. B. Mullins, *J. Mater. Chem. A* **2019**, *7*, 17782.

[12] Z. Zhang, Y. Li, R. Xu, W. Zhou, Y. Li, S. T. Oyakhire, Y. Wu, J. Xu, H. Wang, Z. Yu, *Science* **2022**, *375*, 66.

[13] a) J. Zhao, J. Sun, A. Pei, G. Zhou, K. Yan, Y. Liu, D. Lin, Y. Cui, *Energy Storage Mater.* **2018**, *10*, 275; b) J. Zhang, X. Li, D. Song, Y. Miao, J. Song, L. Zhang, *J. Power Sources* **2018**, *390*, 38; c) H. Yu, H. Dai, Y. Zhu, H. Hu, R. Zhao, B. Wu, D. Chen, *J. Power Sources* **2021**, *481*, 229159; d) Y. Shen, X. Shen, M. Yang, J. Qian, Y. Cao, H. Yang, Y. Luo, X. Ai, *Adv. Funct. Mater.* **2021**, *31*, 2101181; e) Z. Wang, Y. Fu, Z. Zhang, S. Yuan, K. Amine, V. Battaglia, G. Liu, *J. Power Sources* **2014**, *260*, 57; f) J. Zhao, Z. Lu, N. Liu, H.-W. Lee, M. T. McDowell, Y. Cui, *Nat. Commun.* **2014**, *5*, 5088; g) H. Da, S. Pan, J. Li, J. Huang, X. Yuan, H. Dong, J. Liu, H. Zhang, *Energy Storage Mater.* **2023**, *56*, 457; h) T. Feng, Y. Xu, Z. Zhang, X. Du, X. Sun, L. Xiong, R. Rodriguez, R. Holze, *ACS Appl. Mater. Interfaces* **2016**, *8*, 6512; i) S. Heng, L. Lv, Y. Zhu, J. Shao, W. Huang, F. Long, Q. Qu, H. Zheng, *Carbon* **2021**, *183*, 108; j) J. Zhao, Z. Lu, H. Wang, W. Liu, H. W. Lee, K. Yan, D. Zhuo, D. Lin, N. Liu, Y. Cui, *J. Am. Chem. Soc.* **2015**, *137*, 8372.

[14] T. Gao, Y. Han, D. Fraggedakis, S. Das, T. Zhou, C.-N. Yeh, S. Xu, W. C. Chueh, J. Li, M. Z. Bazant, *Joule* **2021**, *5*, 393.

[15] A. Shellikeri, V. Watson, D. Adams, E. E. Kalu, J. A. Read, T. R. Jow, J. S. Zheng, J. P. Zheng, *J. Electrochem. Soc.* **2017**, *164*, A3914.

[16] a) H. Gong, H. Xiao, L. Ye, X. Ou, *Waste Manage.* **2023**, *171*, 292; b) H. F. Li, J. K. Gao, S. L. Zhang, *Chin. J. Chem.* **2008**, *26*, 1585.

[17] Y. Yang, Y. Liu, K. Pu, X. Chen, H. Tian, M. Gao, M. Zhu, H. Pan, *Adv. Funct. Mater.* **2017**, *27*, 1605011.

[18] a) M. Ruska, J. Kiviluoma, VTT Tiedotteita, Espoo, Finland, **2011**; b) L. Chen, K. Wang, X. Xie, J. Xie, *J. Power Sources* **2007**, *174*, 538.

[19] a) S. K. Heiskanen, J. Kim, B. L. Lucht, *Joule* **2019**, *3*, 2322; b) X. Liu, L. Yin, D. Ren, L. Wang, Y. Ren, W. Xu, S. Lapidus, H. Wang, X. He, Z. Chen, G.-L. Xu, M. Ouyang, K. Amine, *Nat. Commun.* **2021**, *12*, 4235; c) H. Yang, H. Bang, K. Amine, J. Prakash, *J. Electrochem. Soc.* **2005**, *152*, A73; d) D. Aurbach, A. Zaban, Y. Ein-Eli, I. Weissman, O. Chusid, B. Markovsky, M. Levi, E. Levi, A. Schechter, E. Granot, *J. Power Sources* **1997**, *68*, 91; e) M. N. Richard, J. R. Dahn, *J. Electrochem. Soc.* **1999**, *146*, 2068.

[20] a) S. Huang, S. Wang, G. Hu, L.-Z. Cheong, C. Shen, *Appl. Surf. Sci.* **2018**, *441*, 265; b) J. Zhang, R. Wang, X. Yang, W. Lu, X. Wu, X. Wang, H. Li, L. Chen, *Nano Lett.* **2012**, *12*, 2153.

[21] M. Gu, A. M. Rao, J. Zhou, B. Lu, *Energy Environ. Sci.* **2023**, *16*, 1166.

[22] X. Liu, J. Liu, T. Qian, H. Chen, C. Yan, *Adv. Mater.* **2020**, *32*, 1902724.

[23] C. Yi, Y. Yang, T. Zhang, X. Wu, W. Sun, L. Yi, *J. Clean. Prod.* **2020**, *277*, 123585.

[24] S. Tu, B. Zhang, Y. Zhang, Z. Chen, X. Wang, R. Zhan, Y. Ou, W. Wang, X. Liu, X. Duan, L. Wang, Y. Sun, *Nat. Energy* **2023**, *8*, 1365.

[25] X. Liu, L. Yin, D. Ren, L. Wang, Y. Ren, W. Xu, S. Lapidus, H. Wang, X. He, Z. Chen, G.-L. Xu, M. Ouyang, K. Amine, *Nat. Commun.* **2021**, *12*, 4235.

[26] Z. Cao, P. Xu, H. Zhai, S. Du, J. Mandal, M. Dontigny, K. Zaghib, Y. Yang, *Nano Lett.* **2016**, *16*, 7235.

[27] M. Winter, P. Novák, A. Monnier, *J. Electrochem. Soc.* **1998**, *145*, 428.

[28] a) X. Ma, M. Chen, B. Chen, Z. Meng, Y. Wang, *ACS Sustainable Chem. Eng.* **2019**, *7*, 19732; b) Y. Gao, C. Wang, J. Zhang, Q. Jing, B. Ma, Y. Chen, W. Zhang, *ACS Sustainable Chem. Eng.* **2020**, *8*, 9447; c) Y.

© 2024 Wiley-VCH GmbH

Zhao, Y. Kang, M. Fan, T. Li, J. Wozny, Y. Zhou, X. Wang, Y.-L. Chueh, Z. Liang, G. Zhou, J. Wang, N. Tavajohi, F. Kang, B. Li, *Energy Storage Mater.* **2022**, *45*, 1092; d) J. Yang, E. Fan, J. Lin, F. Arshad, X. Zhang, H. Wang, F. Wu, R. Chen, L. Li, *ACS Appl. Energy Mater.* **2021**, *4*, 6261; e) B. Markey, M. Zhang, I. Robb, P. Xu, H. Gao, D. Zhang, J. Holoubek, D. Xia, Y. Zhao, J. Guo, M. Cai, Y. S. Meng, Z. Chen, *J. Electrochem. Soc.* **2020**, *167*, 160511; f) W. Chen, R. V. Salvatierra, J. T. Li, C. Kittrell, J. L. Beckham, K. M. Wyss, N. La, P. E. Savas, C. Ge, P. A. Advincula, P. Scotland, L. Eddy, B. Deng, Z. Yuan, J. M. Tour, *Adv. Mater.* **2023**, *35*, 2207303; g) S. Rothermel, M. Evertz, J. Kasnatscheew, X. Qi, M. Grützke, M. Winter, S. Nowak, *ChemSusChem* **2016**, *9*, 3473; h) H. Wang, Y. Huang, C. Huang, X. Wang, K. Wang, H. Chen, S. Liu, Y. Wu, K. Xu, W. Li, *Electrochim. Acta* **2019**, *313*, 423; i) H. Xiao, G. Ji, L. Ye, Y. Li, J. Zhang, L. Ming, B. Zhang, X. Ou, *J. Alloys Compd.* **2021**, *888*, 161593.

[29] a) Q. Dai, J. Spangenberger, S. Ahmed, L. Gaines, J. C. Kelly, M. Wang, *Argonne National Lab.(ANL)*, Argonne, IL, USA, **2019**. b) H. Zhang, Y. Ji, Y. Yao, L. Qie, Z. Cheng, Z. Ma, X. Qian, R. Yang, C. Li, Y. Guo, *Energy Environ. Sci.* **2023**, *16*, 2561; c) Y. Guo, C. Guo, P. Huang, Q. Han, F. Wang, H. Zhang, H. Liu, Y.-C. Cao, Y. Yao, Y. Huang, *eScience* **2023**, *3*, 100091; d) Y. Ji, D. Yang, Y. Pan, Z. Liu, Z. Zhu, X. Qi, M. Ma, R. Jiang, F. Yang, K. Shi, *Energy Storage Mater.* **2023**, *60*, 102801.

© 2024 Wiley-VCH GmbH

15214095, 0, Downloaded from https://onlinelibrary.wiley.com/doi/10.1002/adma.202312548 by Shanxi University, Wiley Online Library on [01/04/2024]. See the Terms and Conditions (https://onlinelibrary.wiley.com/terms-and-conditions) on Wiley Online Library for rules of use; OA articles are governed by the applicable Creative Commons License